Control of thermodynamic liquid-liquid phase transition in a fragility-tunable glassy model

Hai-Rong Qin,[1] Chun-Shing Lee,[2,3] and Yong-Jun Lü[1,*]
[1]*School of Physics, Beijing Institute of Technology, Beijing 100081, China*
[2]*Department of Applied Physics, Hong Kong Polytechnic University, Hong Kong, China*
[3]*Department of Physics, Harbin Institute of Technology, Shenzhen 518055, China*

(Received 15 June 2023; accepted 12 October 2023; published 1 November 2023)

We propose a distinguishable-particle glassy model suitable for the molecular dynamics simulation of structural glasses. This model can sensitively tune the kinetic fragility of supercooled liquids in a wide range by simply changing the distribution of particle interactions. In the model liquid, we observe the occurrence of thermodynamic liquid-liquid phase transitions above glass transition. The phase transition is facilitated by lowering fragility. Prior to the liquid-liquid phase transition, our simulations verify the existence of a constant-volume heat capacity maximum varying with fragility. We reveal the characteristics of the equilibrium potential energy landscape in liquids with different fragility. Within the Gaussian excitation model, the liquid-liquid transition as well as the response to fragility is reasonably interpreted in configuration space.

DOI: 10.1103/PhysRevE.108.055301

I. INTRODUCTION

Although great theoretical and experimental attempts have been made to understand the nature of glass transition, the thermodynamic representation remains a controversial topic. Phenomenally, liquids fall out of equilibrium into a dynamically arrested state when cooled to low temperatures if crystallization is avoided. Based on the steepness of the temperature dependence of structural relaxation time or viscosity, Angell has proposed the well-known classification of liquids: *strong* and *fragile* [1–3]. The former behaves in a nearly Arrhenius fashion and the latter shows a super-Arrhenius increase. The liquid exhibits rich and intriguing dynamic phenomena including multiscale relaxation processes and dynamic heterogeneity as approaching glass transition [4–7]. From the viewpoint of thermodynamics, the excess entropy of a liquid relative to its crystal counterpart decreases with supercooling. Extrapolating the excess entropy down to very low temperature predicts its vanishing at a nonzero temperature, so-called Kauzmann temperature T_K, if the glass transition does not intervene [8]. A possible solution is that the supercooled liquid is fated to be terminated by a thermodynamic phase transition to an ideal glass above T_K.

The theoretical justification of the thermodynamic liquid-glass phase transition mostly relies on the potential energy landscape (PEL) approach. The Gaussian excitation model, which is developed by modifying earlier two-state models with considering interactions between configurational excitations [9,10], proposes the thermodynamic conditions for the occurrence of liquid-glass transition. It is allowable that the transition occurs above T_g, namely the liquid-liquid phase transition (LLPT). The LLPT may be one of the most controversial problems in glassy physics. It has been frequently claimed in a variety of liquids ranging from model liquids [11], network-forming liquids [12–14], and polymers [15,16] to metallic and oxide melts [17,18], whereas explanations on its nature seem diverse. The light-scattering experiments have observed large-scale density fluctuations in highly supercooled polymers, which is believed to be due to the presence of LLPT hidden in spinodal decomposition [19]. Tanaka has suggested that the LLPT associated with the critical-like instability may exist in any liquids [20]. Recent simulations propose a dynamical liquid-glass transition in trajectory space in contrast to the conventional knowledge in configuration space [21,22].

Unifying thermodynamic and dynamic representations always motivates the study on glass transition. For example, the Adam-Gibbs relation provides a connection between the relaxation time and the configurational entropy of supercooled liquids [23]. Taking an overview of reported experimental results, most known LLPT in strong liquids are at high temperatures, suggesting that there is a relevance between LLPT and fragility. In this paper, we propose a distinguishable-particle glassy model (DPGM) which can tune the kinetic fragility by controlling a thermodynamic potential parameter. By using a hybrid of swap Monte Carlo (MC) simulation and molecular dynamics (MD) simulation, we observe the thermodynamic liquid-liquid transition in a wide range of fragility, and shed light on the connection between LLPT and fragility based on PEL.

II. COMPUTATIONAL METHODS

A. Distinguishable-particle glassy model

We use the DPGM to prepare the tunable-fragility glass-former. This model is developed from the distinguishable-particle lattice model (DPLM) proposed in Refs. [24,25], and is suitable to perform MD simulations. A thermodynamic

*yongjunlv@bit.edu.cn

system consisting of N distinguishable particles labeled from 1 to N is prepared in three dimensions (3D). The N particles are randomly grouped in two species with different size: 80% large (group A) and 20% small (group B) particles. The interaction ϕ_{ij} between any two particles i and j separated by a distance r follows the Lennard-Jones (LJ) potential form

$$\phi_{i_\alpha j_\beta} = -4V_{ij}\left[\left(\frac{\sigma_{\alpha_i\beta_j}}{r}\right)^{12} - \left(\frac{\sigma_{\alpha_i\beta_j}}{r}\right)^{6}\right], \tag{1}$$

where α,β = A,B, and the distance cutoff is 2.5. The depth of potential well V_{ij} for the interaction between particle i and j is randomly sampled within $[V_0,V_1] = [0.25,1.25]$ following a bicomponent distribution function $g(V_{ij})$ prior to simulations

$$g(V_{ij}) = \frac{G_0}{\Delta V} + (1 - G_0)\delta(V_{ij} - V_0), \tag{2}$$

where $\Delta V = V_1 - V_0 = 1$ and δ is the Dirac function. The distribution function $g(V_{ij})$ is a sum of a uniform and a delta term. The parameter $G_0 \in [0, 1]$ is the probabilistic weight of the uniform distribution. Actually, it determines the appearance of PEL, and also controls the kinetic fragility as shown in the following sections. For $G_0 = 1$, Eq. (2) reduces to the uniform distribution; for $G_0 = 0$, all the particle pairs have the same LJ energy parameter V_0. The distance parameter σ is given by the Kob-Anderson model: $\sigma_{AA} = 1$, $\sigma_{BB} = 0.88$, $\sigma_{AB} = 0.8$ [24]. This strategy can effectively avoid crystallization in quenching.

The distinguishable-particle model provides a numeric model for real polydispersive systems, in particular it is analogous to high-entropy alloys in the limit of atomic species. Different from the void dynamics of crystalline lattice in DPLM, the DPGM faithfully produces the particle trajectory, which is expected to directly simulate the structure and dynamics of very complex disordered systems. Our distinguishable-particle model differs significantly from the size-polydisperse model in the correlation among interactions. Due to well depths, V_{ij} and V_{ik} for particle i paired with particles j and k are independent random variables in the distinguishable-particle model, the correlation has been eliminated, and thus the kinetic fragility is expected to be tuned by changing simply interaction distributions. In contrast, the size-polydisperse model shows strong interaction correlation given a size distribution, and the fragility as high as the present DPGM is difficult to be achieved.

B. Molecular dynamics simulations

MD simulations are performed in the canonical ensemble (NVT). In the initial configuration, 4000 particles are arranged into the face-centered cubic lattice with the number density of 1.69. It is then relaxed for 10^7 MD steps at high temperatures to achieve equilibrium liquid systems. The periodic boundary conditions are applied in the three dimensions. The time step is 0.002 in reduced unit. All the particles have the same mass. To reach the equilibrium state at low temperatures, we use a two-step simulation procedure: a hybrid MC swap/MD and a conventional MD relaxation. First, a sequence of MC blocks consisting of 10 MC swaps each are carried out, which are separated by several MD blocks consisting of 100 runs each. The total MD steps reach 10^7. Then, a long-time MD relaxation consisting of 4×10^7 MD steps is performed. A Verlet algorithm is used for the integration of the motion equation. The thermostat of Nosé and Hoover introduced by Melchionna has been used in the simulations [25,26]. All simulations are performed using an in-house code interfacing with LAMMPS software package [27].

C. Swap Monte Carlo simulations

To speed up the equilibration process, a hybrid scheme consisting of alternating between conventional MD sequences and particle swap MC sequences is used as mentioned above. This scheme has been proved to improve the numerical efficiency for producing equilibrium configurations of model glassformers at low temperature [28]. At each end of MD block (100 MD steps), the simulation time is paused, and the particle positions and velocities are frozen. Then a swap MC block composed of 10 swaps is performed. In each swap, a particle pair is randomly selected from all particle pairs with equal probability, and the exchange of their types together with particle size is accepted or rejected based on the Metropolis probability at T. Here the particle type is in accordance with the particle ID sequentially. The swap moves are beneficial for the equilibrium sampling of phase space in the NVT ensemble.

III. RESULTS AND DISCUSSION

A. Tunning fragility in DPGM

We choose six G_0 values, $G_0 = 1$, 0.7, 0.4, 0.1, 0.03 and 0.01, ranging from the system with complex particle interactions to the nearly identical-particle system. These systems are quenched into glass states from high temperatures and crystallization never occurs. Figure 1(a) shows the temperature dependence of potential energy at various G_0. In the whole temperature range we studied, the potential energy is consistently raised with decreasing G_0. The temperature derivatives reach a maximum as the temperature reduces at each G_0, and thus the calorimetric glass transition temperature T_g is approximately determined based on it. Figure 1(b) shows that T_g decreases from 1.20 to 0.52 in reduced LJ unit when G_0 decreases from 1 to 0.01, exhibiting a good glass forming ability covering a wide T_g range. Although the potential energy keeps increasing with decreasing G_0, the growth is slowed down in low G_0 region. Accordingly, the temperature dependence of T_g becomes weak so that an exponential relation is approximated over the whole G_0 range, as shown in Fig. 1(b). We further isothermally relax the liquid until equilibrium liquid state is achieved. The equilibrating scheme includes two stages, a hybrid MC/MD swap algorithm followed by a long-time MD relaxation. Theoretically, for a distinguishable-particle system, the particles arrange at equilibrium in such way that the depth of potential well V_{ij} follows *a posteriori* distribution [29,30]

$$p_{\rm eq}(V) = g(V)\exp(-V/k_BT)/\Lambda, \tag{3}$$

where $\Lambda = \int dV\, g(V)\exp(-V/k_BT)$ is the normalization factor. In simulations, the distance cutoff for sampling V_{ij} is 1.3σ that is equivalent to the distance at the first peak in total

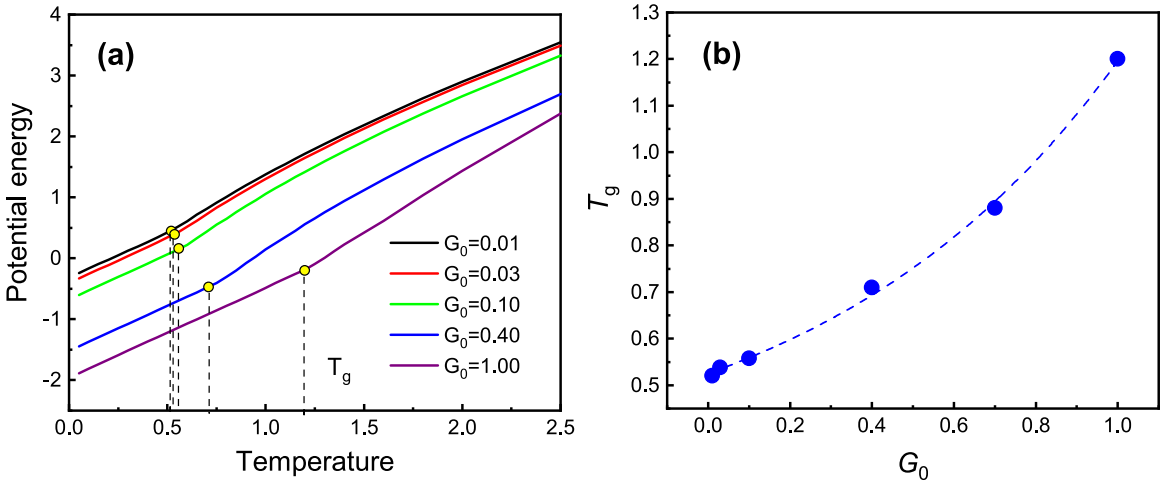

FIG. 1. Potential energy and glass transition temperature. (a) Potential energy as a function of temperature at different G_0. (b) Glass transition temperature versus G_0. The dashed line is an exponential fit.

radial distribution function curve. We check the distributions of V_{ij} and they are in good agreement with the theoretical prediction of equilibrium states [Eq. (3)] at various G_0 and even at the temperatures close to T_g, as shown in Fig. 2. The following results and discussion are exactly in thermodynamic equilibrium states. The structural relaxation is measured by

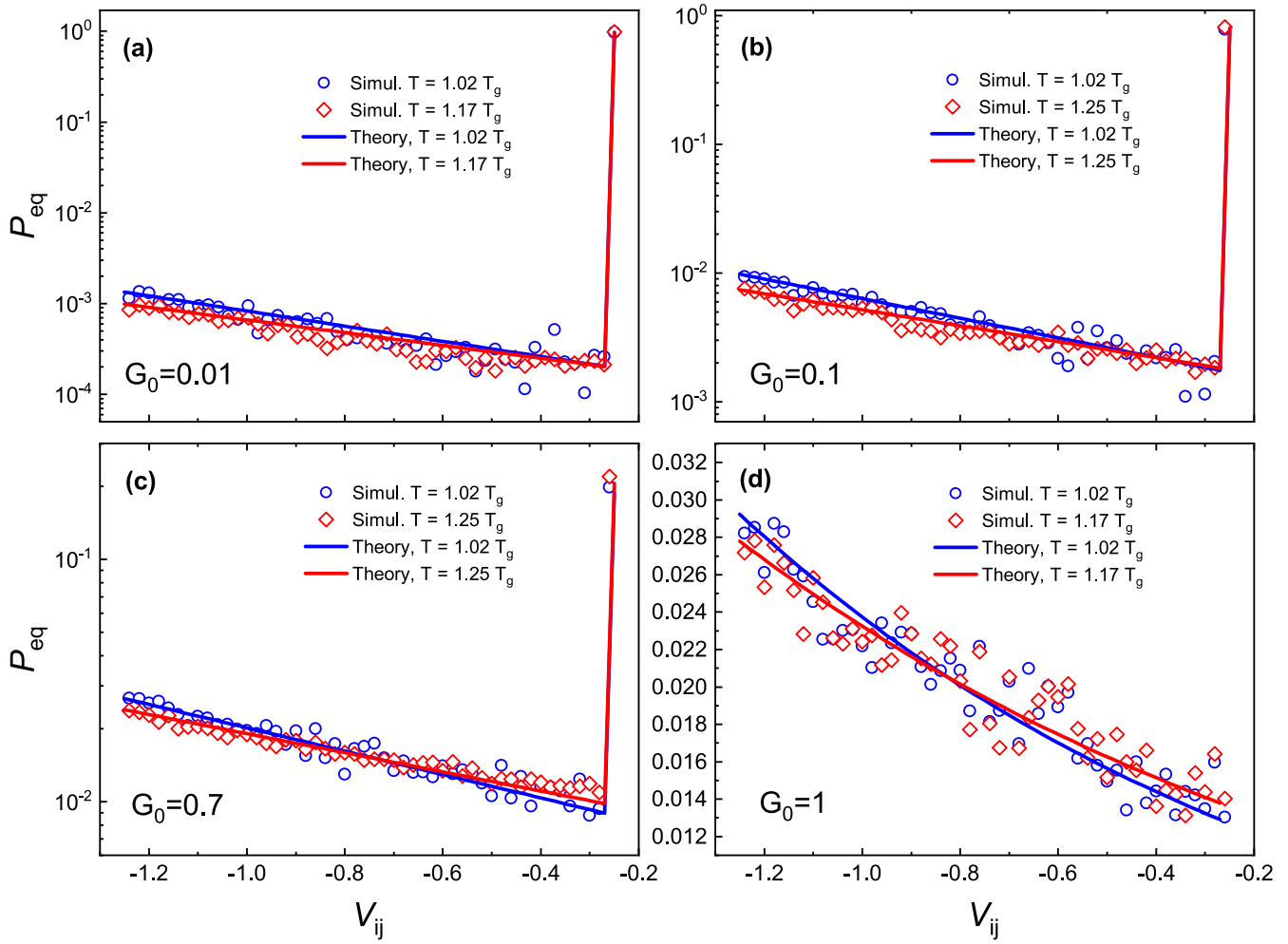

FIG. 2. Distributions of the depth of potential wells at equilibrium states at $T = 1.17$ and $1.02\ T_g$ for (a) $G_0 = 0.01$, (b) $G_0 = 0.1$, (c) $G_0 = 0.7$, and (d) $G_0 = 1$.

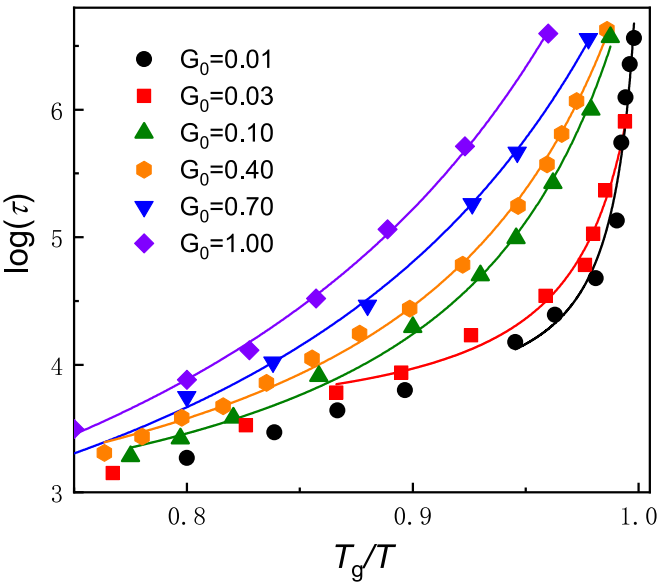

FIG. 3. Structural relaxation time versus T_g/T at various G_0. The solid lines are fits to the VFT law.

the self-intermediate scattering function (SISF)

$$F_s(q,t) = \frac{1}{N}\sum_{j=1}^{N}\langle \exp\{i\boldsymbol{q}[\boldsymbol{r}_j(t) - \boldsymbol{r}_j(0)]\}\rangle, \tag{4}$$

where r_j is the position vector of particle j, and the wave number $\boldsymbol{q}$ is determined by the location of the first peak of the structure factor. The structural relaxation time τ_α, which is evaluated by fitting SISF to a stretched exponential $\varphi(t) = A\exp[-(t/\tau_\alpha)^\gamma]$, is plotted against the inverse of temperature, as shown in Fig. 3, where γ is the stretching exponent. The relaxation time τ_α increases in a super-Arrhenius fashion with decreasing T, which is well fitted by the Vogel-Fulcher-Tamman law (VFT) $\tau_\alpha = \tau_0\exp[BT_0/(T - T_0)]$, as approaching T_g. The super-Arrhenius behavior is increasingly enhanced as G_0 decreases. The deviation from the Arrhenius law is measured by the kinetic fragility m_d which is defined as $m_d = \partial \log(\tau_\alpha)/\partial(T_g/T)|_{T=T_g}$. It is shown that m_d dramatically increases from 29 to 221 when G_0 is decreased from 1 to 0.01, and they approximately follow an inverse relation, as shown in Fig. 4. In fact, realizing the fragility tuning in a glass family has been suggested in several ways. For example, in hard polyhedron glass formers, the fragility has been found to sensitively depend on the particle shape [31]. In Mg-Cu-Y alloys, a variation of fragility over 16–46 is achieved by 25% at composition change [32]. Corresponding to real systems, the present fragility covers most glassformers available in experiments ranging from *strong* network-forming liquids such as silica ($m_d \approx 20$) to *fragile* polymers ($m_d > 200$) [33]. Thus, DPGM exhibits a good ability of tuning fragility in a wide range by simply controlling G_0. In addition, the relaxation time diverges at T_0 as suggested by the VFT law. Figure 5 presents the fitted T_0 as a function of G_0. Similar to the G_0 dependence of T_g, T_0 reduces with decreasing G_0 following an exponential law. It is close to T_g, and moreover, the gap between them is narrowed as G_0 decreases, which suggests

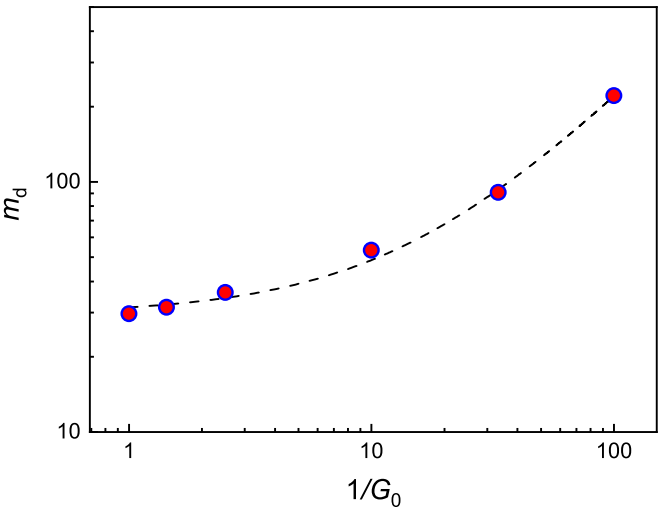

FIG. 4. Logarithmic plot of the correlation between the kinetic fragility m_d and the inverse of G_0. The dashed line is a linear fit.

a good correlation between the calorimetric and the dynamic glass transition in distinguishable-particle liquids.

B. Fragility dependence of the liquid-liquid transition

We calculate the constant-volume heat capacity C_V by the energy fluctuation $C_V = N(\langle U^2\rangle - \langle U\rangle^2)/k_BT^2$, where U is the internal energy. Figure 6 shows that C_V has a broad maximum before drop at T_g. The heat-capacity maximum has been predicted in various excitation state models, and it is also verified in some strong liquids associated with LLPT, such as water [34–36]. We find that the rise of heat capacity after passing through the maximum are not continuous. It implies the possibility of a thermodynamic transition following the heat-capacity maximum. To further clarify, we examine the variation of internal energy with temperature, as shown in Fig. 7. It definitely displays an abrupt drop close to the C_V maximum. These thermodynamic response behaviors support the existence of the first-order LLPT. The energy

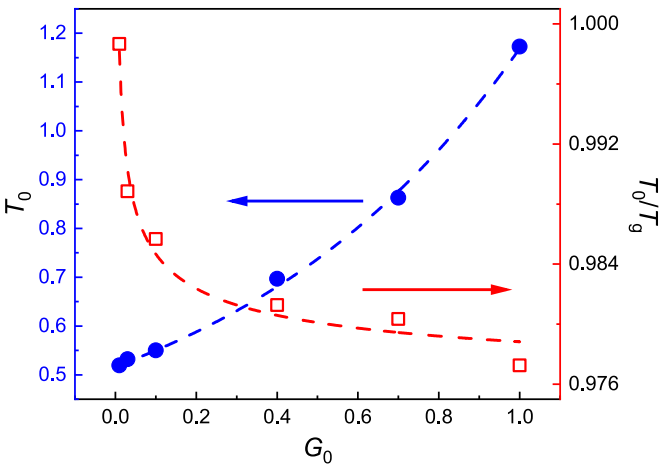

FIG. 5. VFT singularity temperature T_0 as a function of G_0. The plot on the right y axis shows the results scaled by the glass transition temperature T_g.

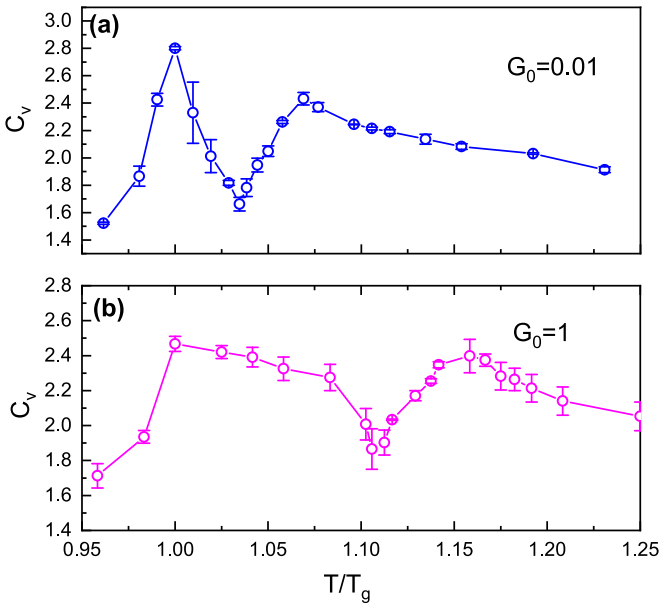

FIG. 6. Constant-volume capacity as a function of T/T_g at (a) $G_0 = 0.01$ and (b) $G_0 = 1$.

change through the transition is less than 0.02, which is much smaller than the value of 0.3 for crystallization in DPGM, exhibiting a characteristic feature of weak first-order phase transition. Here we attempt to understand LLPT from configuration space. More than 1000 configurations are sampled randomly from an additional MD trajectory consisting of 10^7 steps at each temperature and then the energy minimization is performed using the conjugate gradient algorithm to ensure them in basins of PEL (inherent structure). We assume that most basins can be visited in the long-time MD run and these minimized configurations therefore approximately represent the topography of PEL. Energy minimization lowers the average internal energy but does not affect the structure of PEL. Figures 8(a)–8(c) show the distributions of basin energy ϕ towards T_g at $G_0 = 1$, 0.1, and 0.01. The distribution is approximated by a Gaussian function

$$P(\phi) \propto \exp\left(-\frac{(\phi - \phi^*)^2}{2\Gamma^2}\right), \tag{5}$$

with the average basin energy ϕ^* and the variance Γ. The Gaussian-type distribution shifts to lower energies with decreasing temperature until a bimodal distribution forms. We find that the bimodal mode is not held at a well-defined temperature but covers a temperature range, below the lower boundary of which the single Gaussian distribution is recovered. Most bimodal distributions are sensitive to the thermal history: they depend on the waiting time prior to sampling, which is more pronounced in fragile systems and reflects the instability of PEL.

Clearly, the bimodal characteristic in ϕ distributions manifests the coexistence of two liquid phases distinguished by high- and low-energy state. It provides the solid evidence that the LLPT observed in DPGM liquids is the thermodynamic first order, which is coincided with the results suggested by C_V and U. Tanaka *et al*. have classified LLPT into nucleation-growth type and spinodal-decomposition type based on their early experiments [37]. In this work, the fluctuations of ϕ distributions actually imply that the present LLPT features a spinodal-assisted transition. Due to hiding in the spinodal region, the LLPT temperature T_{LL} is difficult to be accurately determined. Here we extend the MD trajectory to that consisting of 10^8 steps and check the distribution of basin energies at

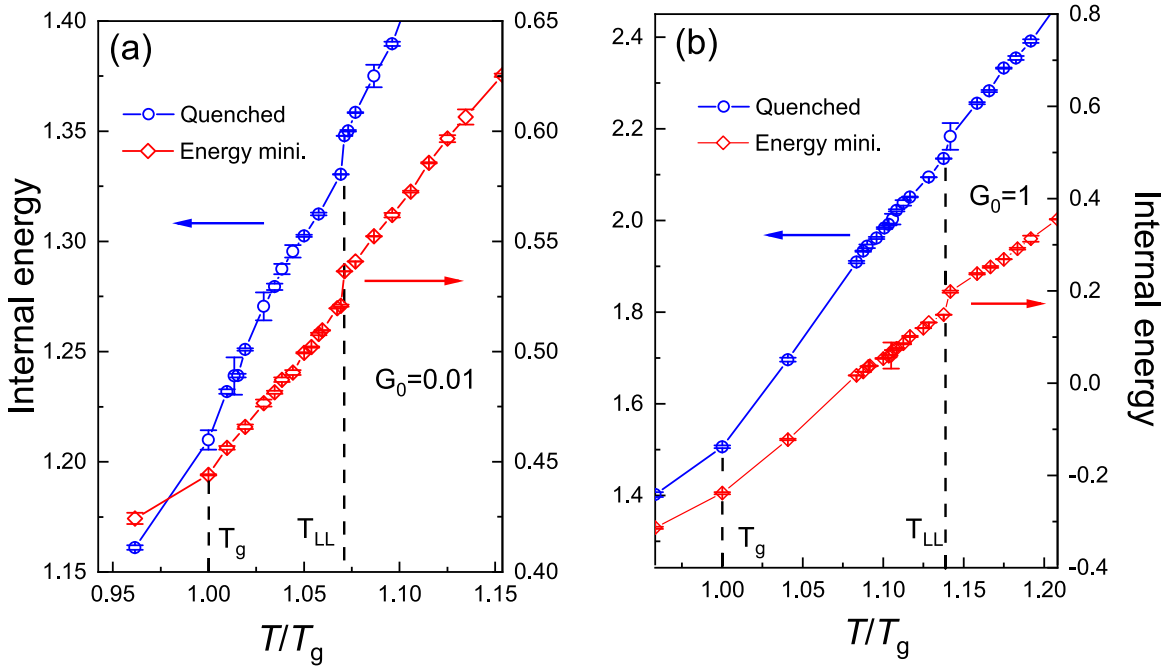

FIG. 7. Internal energy as a function of scaled temperature for the quenched system and the energy-minimized system. (a) $G_0 = 0.01$; (b) $G_0 = 1$.

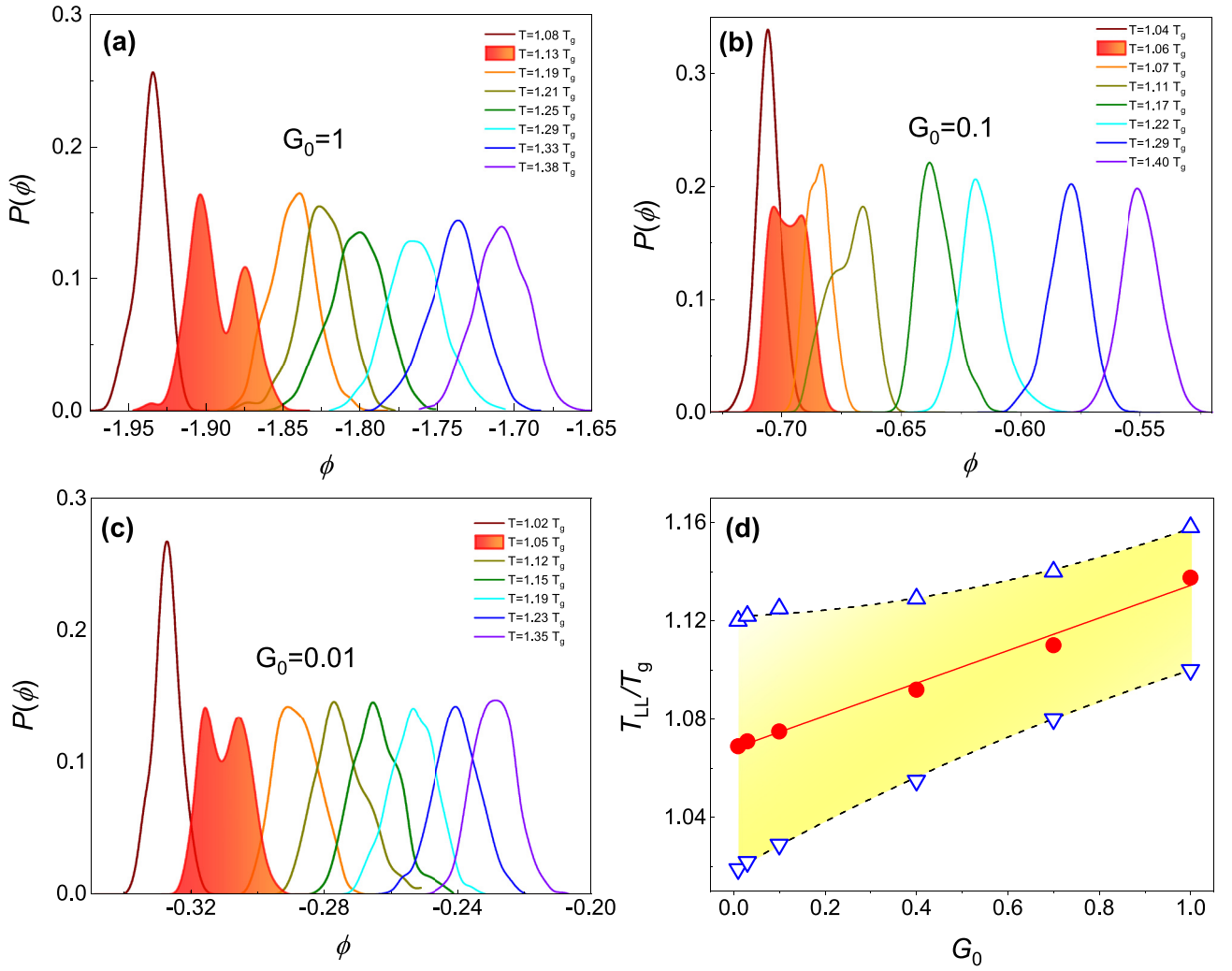

FIG. 8. Distributions of basin energy at various temperatures and at (a) $G_0 = 0.01$, (b) 0.1, and (c) 1. The bimodal distributions highlighted by filled curves indicate the stable coexistence of the high-energy and the low-energy liquid state, and the corresponding temperature is identified as the LLPT temperature. (d) The scaled liquid-liquid transition temperatures versus G_0 (solid symbols). The cross symbols are results predicted by the Gaussian excitation model. The upper and lower spinodal instability temperatures are plotted as open symbols.

different waiting time. If it is stable, namely less dependent on waiting time, the temperature is approximated by T_{LL}, as shown in Appendix A. In addition, from the distribution evolution, we are allowed to estimate empirically the spinodal region: the temperatures corresponding to the first emergence and vanishing of the bimodal distribution are approximated as upper and lower spinodal temperature. Figure 8(d) plots the G_0 dependence of T_{LL} in the spinodal region. As the fragility is enhanced, the transition temperature scaled by T_g is reduced linearly, meanwhile, the spinodal domain expands.

The two-state model describes a glass as the system composed of some particles in excitation statelike defects in crystals relative to the ground state in ideal glass. The Gaussian excitation model assumes that the ϕ distribution follows a Gaussian function in contrast to a delta function in the original two-state model, though more precisely, it is asymmetric due to the low-energy-side preference of excitation states. By fitting to the Gaussian function, the temperature variation of average basin energies above T_{LL} is plotted in Fig. 9. The average basin energy monotonically decreases with temperature for all the cases of G_0. Moreover, more fragile systems have higher average basin energies but weaker temperature dependence. In the excitation model, the average basin energy is given by $\phi^* = x\varepsilon_0$, where x is the concentration of excited particles, ε_0 is the excitation energy per particle [9]. If the interactions between excitation states are considered, ϕ^* is rewritten as

$$\phi^* = x\varepsilon_0 - 2\lambda, \tag{6}$$

where the parameter λ is a measurement of the average interaction energy between configurational excitations [9,10]. The concentration-dependent average interaction energy is given by

$$\lambda_0(x) = (1-x)^2\lambda_1 + x^2\lambda_2, \tag{7}$$

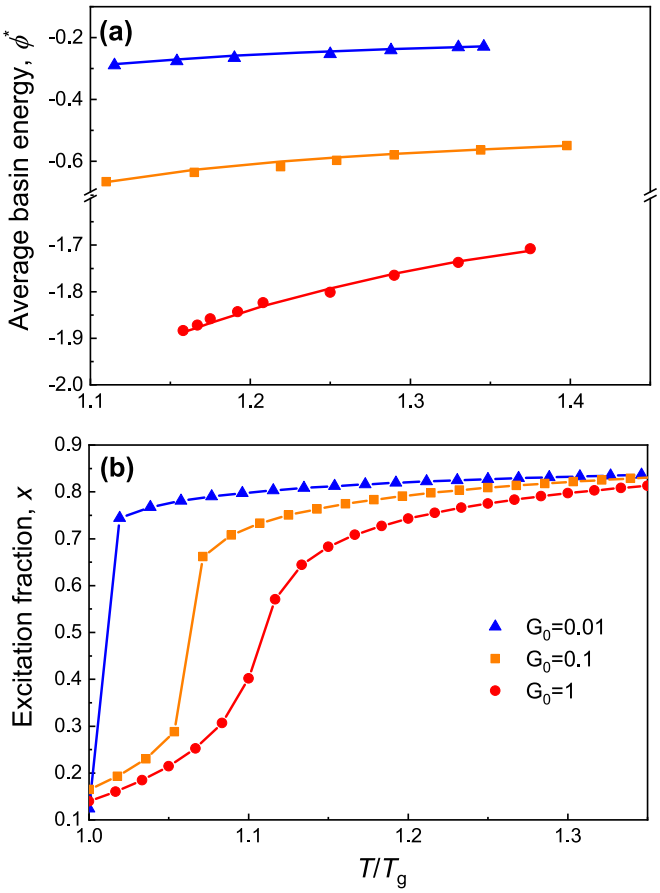

FIG. 9. (a) Average basin energy as a function of temperature for $G_0 = 1$, 0.1, and 0.01. The solid lines are fits to the Gaussian excitation model. (b) The fraction of particles in excitation state versus temperature at $G_0 = 1$, 0.1, and 0.01.

where λ_1 and λ_2 are the coupling parameter, representing the interaction energy on ground and excitation states. It has been confirmed that the contribution of the interaction energy on the ground state(λ_1) can be neglected without reducing the quality of fit [10]. Therefore, we only consider the second term on the right side of Eq. (7) in fitting. The concentration of excitation states x is given by a self-consistent equation

$$x = [1 + e^{-s_0+\beta(\varepsilon_0-2x\lambda)}]^{-1}, \tag{8}$$

where s_0 is the entropy change per particle due to yielding an excitation and $\beta = 1/k_BT$. This model well fits the average basin energies in simulations with the assumption that the interaction energy λ is independent of temperature, as solid curves shown in Fig. 9(a), which allows us to understand the relationship between fragility and LLPT in configuration space. The results indicate that almost all the particles are configurationally excited in fragile systems and the population of excited states is less affected by temperature until it drops at LLPT, as demonstrated in Fig. 9(b). In contrast, for low-fragility liquids, the excited-state concentration is reduced following a power law and then exponentially decays after the drop at LLPT. The drop behavior is expected to approach the limit of inflection point as the fragility vanishes. The fitted excitation energy ε_0 grows from 2.38 for $G_0 = 0.01$ to 6.22 for $G_0 = 1$. Table I lists ε_0, s_0, and λ_2 in the Gaussian excitation model by fitting to the basin energies for different G_0 cases. These parameters reflect that the PEL of strong liquids is characterized by a number of deeper basins but it is less rugged for fragile ones.

TABLE I. The excitation energy ε_0, the excitation entropy s_0, and the interaction energy λ at various G_0. They are calculated by fitting to the Gaussian excitation model.

G_0	ε_0	s_0	λ
0.01	2.38	2.02	1.22
0.03	2.45	2.14	1.23
0.1	2.70	2.48	1.26
0.4	3.84	2.70	1.74
0.7	5.02	2.76	2.34
1	6.22	2.78	2.52

With increasing G_0, the excitation entropy s_0 increases from 2.02, 2.48, to 2.78 at $G_0 = 0.01$, 0.1, and 1. If the vibrational contribution is ignored, the configurational entropy is then approximated by the mixing entropy involving the interaction effect of excitation states

$$s_c = s_0(x) - x^2\lambda/T, \tag{9}$$

where

$$s_0(x) = xs_0 - x\ln x - (1-x)\ln(1-x), \tag{10}$$

if the ideal mixing is assumed. Figure 10 shows that the high-G_0 system has higher configurational entropy. It means that the tunability of fragility in DPGM, more essentially, is accomplished by tuning entropy: increasing G_0 diversifies the potential well depth and wrinkles the PEL, resulting in the rise of s_c. When the Gibbs free-energy difference between two liquid phases vanishes, the equilibrium phase transition temperature is given by

$$T_{LL} = (\varepsilon_0 - \lambda)/s_0 \tag{11}$$

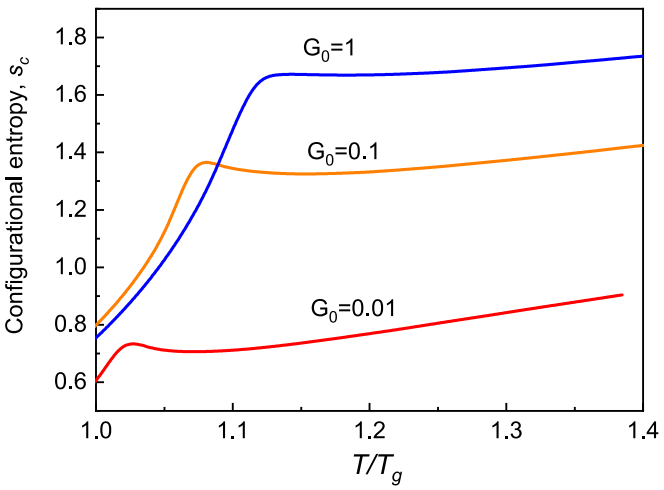

FIG. 10. Configurational entropy as a function of temperature predicted by the Gaussian excitation model.

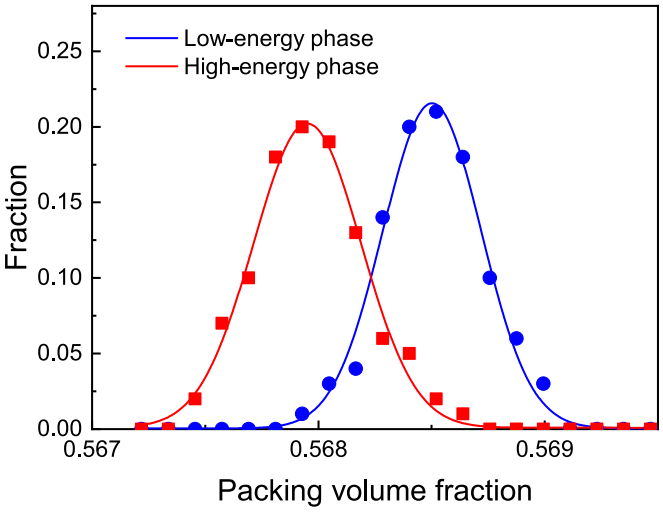

FIG. 11. Distributions of the packing volume fraction for the low- and high-energy phase for $G_0 = 0.01$. The solid lines are the Gaussian fits.

in the Gaussian excitation model. Using the fitted ε_0, λ, and s_0, the prediction agrees with our simulations [Fig. 8(d)]. From the above equation, the LLPT temperature is determined by the competition between the effective excitation energy $\varepsilon_0 - \lambda$ and the excitation entropy s_0. In fact, they all increase with increasing G_0 in DPGM, whereas ε_0 more sensitively depends on G_0 compared to λ and s_0. Thus it is the excitation energy ε_0 that dominates T_{LL}. For strong liquids, large excitation energy is responsible for high phase-transition temperature. On the other hand, the concentration of excitation states x plays a crucial role in understanding the temperature behavior of C_V. In the Gaussian excitation model, the primary contribution to C_V is given by $x^2\lambda/T$. Thus, the decrease in x suppresses the rise of C_V on cooling, resulting in the C_V maximum above T_g. Once the LLPT occurs, C_V drops to a low value representative of low-energy phase. For fragile liquids, this drop is closer to the C_V maximum owing to the weak temperature dependence of x upon LLPT. It agrees with the simulation result that C_V shows steeper descent after passing through the maximum for fragile liquids (Fig. 6). The LLPT observed in tetrahedral liquids is commonly characterized by the transition between high-density and low-density phases [38,39]. Due to the constraint of NVT ensemble, the global density cannot be served as order parameter for the present case. However, we still observe a preference of local density associated with LLPT. Although the radial distribution functions (RDF) and structure factors indicate nearly identical global structure between the high- and the low-energy state, as shown in Appendix B, a slight difference is found within the nearest neighboring distance: the low-energy phase has higher local density compared to the high-energy phase (the coordinate number is 5.3 and 5.2, respectively). More definite evidence comes from the local packing fraction around a given particle, which is defined as the volume fraction of surrounding particles within the sphere with a radius cutoff of 2.5, where the particle diameter is approximated by the first-peak position of partial RDFs. Figure 11 plots the distributions of the local packing fraction for the low- and high-energy phases. Two Gaussian-like distributions are clearly distinguished despite that the difference in average value is tiny (<0.1%). We also analyze the locally structural characteristics using the Voronoi tessellation method [40] and do not find visible locally structural preference across LLPT (see Fig. 14 in Appendix B). Along with the increasing degree of dense packing across LLPT, the pair interactions are found to be rearranged. We calculate the radial distribution of the depth of potential wells V_{ij} through LLPT (Fig. 15 in Appendix B) and find that high-V_{ij} pairs are more preferred to assemble in the nearest neighboring distance, resulting in formation of the low-energy state. The rearrangement of pair interactions is not very remarkable, which coincides with the weak characteristics of LLPT in this work. For real LLPT systems, the energy drop is more likely attributed by the rearrangement of particle configuration to form some characteristic clusters with local order. Bond ordering across LLPT as well as glass transition in real liquids is worth further investigation.

IV. CONCLUSIONS

In summary, we propose a distinguishable-particle glassy model that exhibits excellent tunability of the kinetic fragility of glassformers. Using MD simulations, the thermodynamic liquid-liquid phase transition is verified to occur above T_g in liquids with different fragility. We provide the quantitative

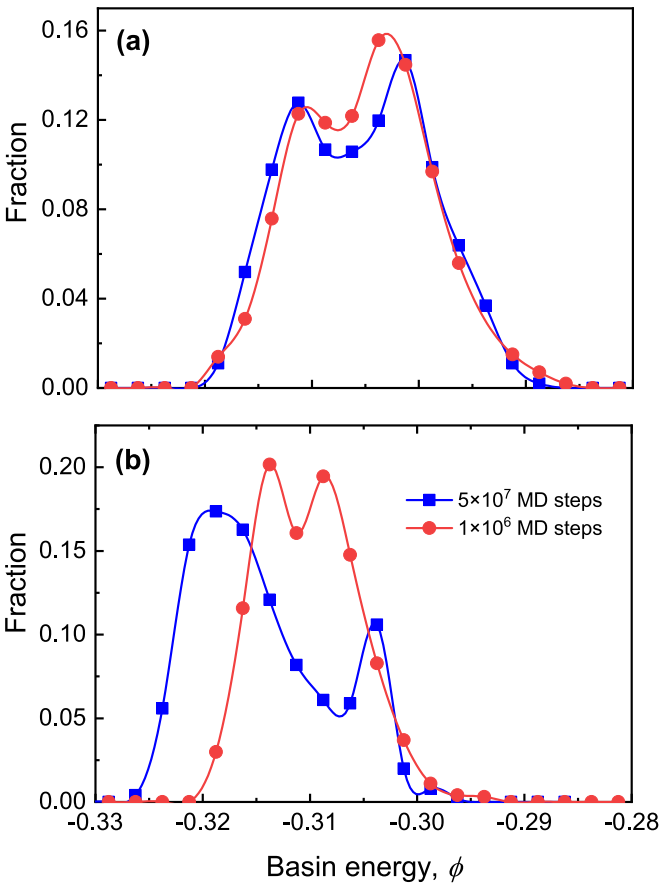

FIG. 12. Distributions of basin energy sampled after 5×10^7 MD steps and 1×10^8 MD steps at $G_0 = 0.01$, respectively. (a) $T = 0.556(T_{LL})$, (b) $T = 0.535(< T_{LL})$, in spinodal decomposition region.

relation between the LLPT and the kinetic fragility. Strong liquids are characterized by deeper basins in PEL; In contrast, fragile liquids show more smooth PEL with weak temperature dependence. Within the framework of the Gaussian excitation model, our simulations suggest that the strong liquids feature high configurational excitation energy that is the dominant factor of facilitating LLPT. However, fragile liquids have a large population of configurational excitation states that are almost temperature independent. These differences well explain the temperature behavior of C_V varying with fragility. The LLPT is reflected by the rise of the packing volume fraction accompanied by the rearrangement of pair interactions. The DPGM provides a promising approach to study the fragility and relevant issues in glass family.

ACKNOWLEDGMENTS

The authors are grateful to Chi-Hang Lam for helpful discussion. This work was supported by the National Natural Science Foundation of China under Contracts No. 52071029, No. 52031016, and Hong Kong General Research Fund Grant No. 15303220. The computer resources at the Shanghai and Tianjin Supercomputer Center are gratefully acknowledged.

APPENDIX A: DETERMINATION OF LIQUID-LIQUID PHASE TRANSITION TEMPERATURE

We determine the liquid-liquid phase transition temperature by examining the stability of the distribution of basin energy. Because the liquid-liquid phase transition occurs in spinodal decomposition region, the thermodynamic distribution displays strong fluctuations with observation time. In this work, we sample the distribution of basin energy after 5×10^7 and 1×10^8 MD steps, respectively. The temperature corresponding to the most stable distribution is approximated as the liquid-liquid transition temperature. For example, Fig. 12 shows the distributions of basin energy at two waiting times and at the liquid-liquid transition temperature. For the sake of comparison, the case at a temperature in the spinodal decomposition regime is also provided.

APPENDIX B: STRUCTURAL ANALYSIS

1. Radial distribution function and structure factors

Radial distribution function (RDF) $g(r)$, which reflects the probability of finding a particle in the volume element $r\ r+dr$ at a distance r from a specified particle. The experimental measured structure factor $S(q)$ is related to RDF by Fourier transformation as

$$S(q) = 1 + \rho \int_V [g(r) - 1] e^{-iqr} dr, \tag{B1}$$

assuming that the system is isotropic. We choose 100 configurations in the low-energy and the high-energy states at T_{LL}, respectively, and calculate $g(r)$ and $S(q)$. Figure 13 presents the total RDF and the structure factors of the low- and high-energy liquid at $G_0 = 0.01$ and 1. Although they indicate nearly identical global structure, slight differences are still visible, particularly within the nearest neighboring distance.

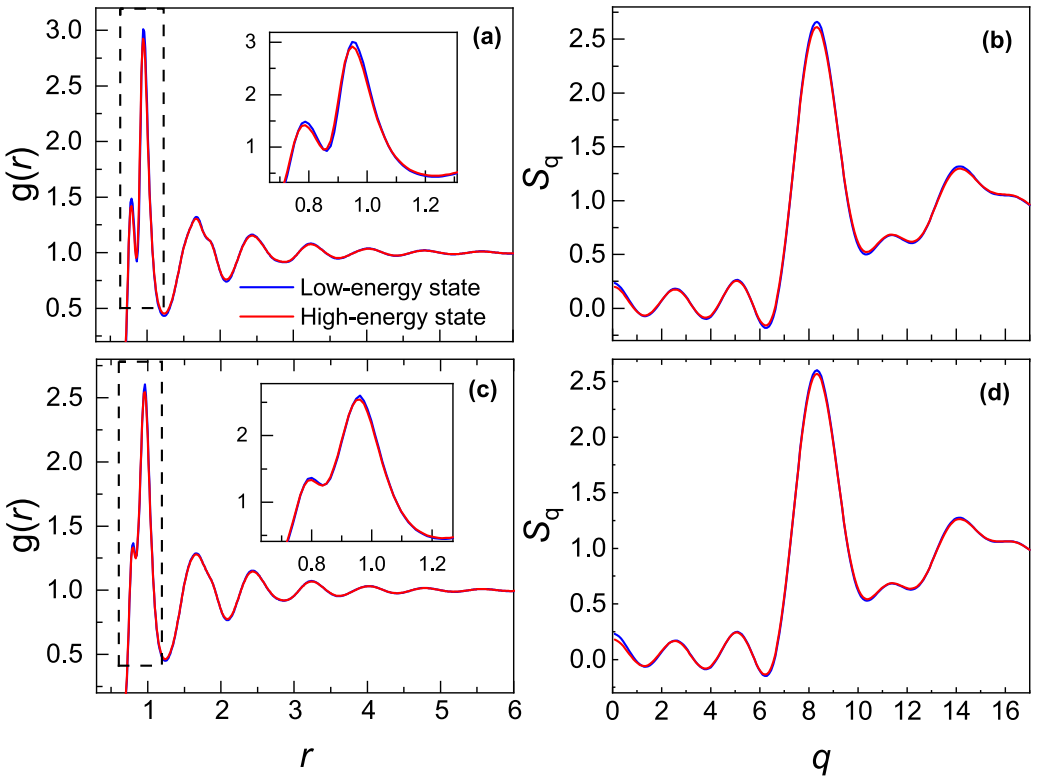

FIG. 13. Radial distribution functions (RDF) and structure factors for the low-energy liquid and the high-energy liquid at $G_0 = 0.01$ (a) and (b), and $G_0 = 1$ (c) and (d). The inset shows the enlarged view in the nearest neighboring distance.

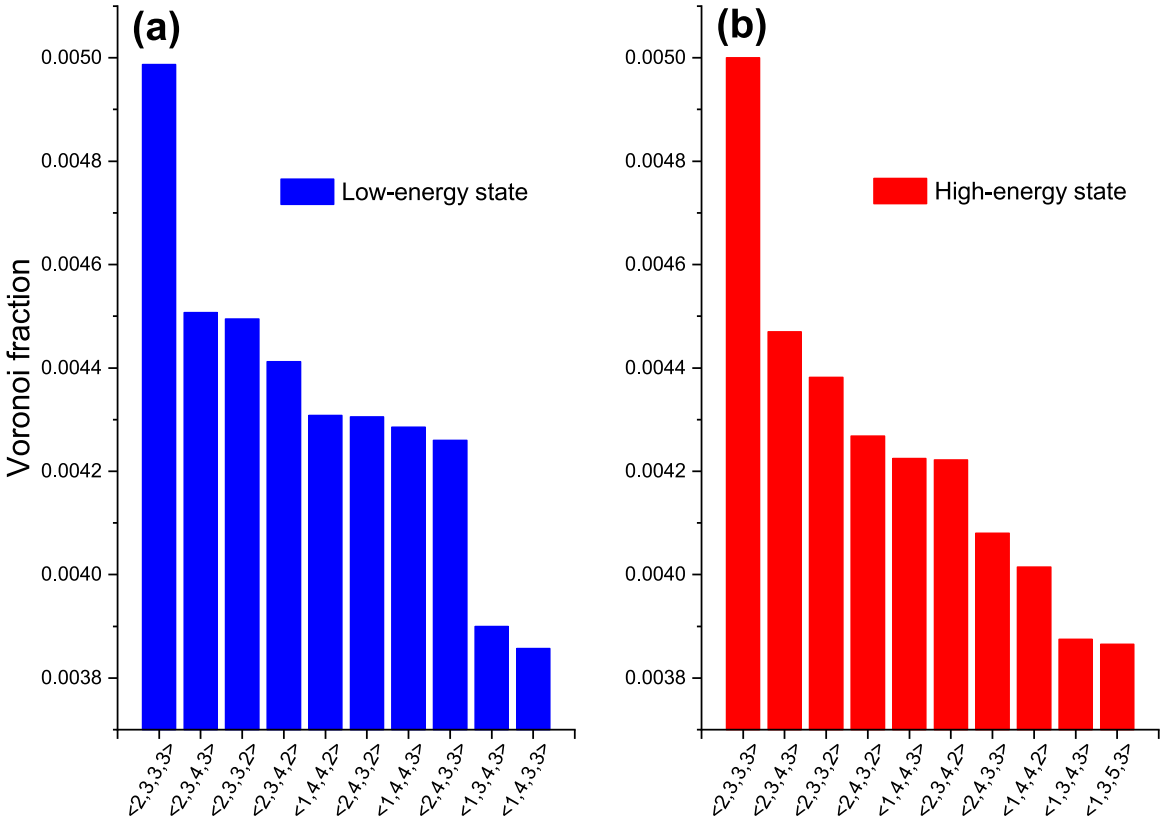

FIG. 14. Top ten Voronoi indices found in (a) the low-energy liquid and (b) the high-energy liquid.

2. Voronoi structure analysis

We use the Voronoi tessellation method to study the local structure through the liquid-liquid phase transition. For each atom, a Voronoi polyhedron is constructed by the mid-perpendicular planes between it and its neighbors. Each Voronoi polyhedron is characterized by the Voronoi index $\langle n_3, n_4, n_5, n_6\rangle$, where $n_i (i = 3, 4, 5, 6)$ is the number of i-edges faces and $\sum n_i$ thus is the coordination number [40]. Figure 14 shows the top ten characteristic indices in the two liquid phases. We do not find the preference of the fivefold symmetric structure that is frequently observed in metallic glass formers. Furthermore, the comparisons between the two liquid phases do not show a remarkable difference in short-range order.

3. Radial distribution of pair interactions

We analyze the average depth of potential wells V_{ij} along the radial direction. Similar to the method used in the calculation of RDF, all particles in the volume element dr at a distance r from a given particle i are found out, and then V_{ij} is averaged over the shell

$$\overline{V}(r) = \frac{\sum_i \sum_j V_{ij}}{N_a}, \tag{B2}$$

where N_a is the number of particle pairs (i, j) separated by $[r, r+dr]$. The cutoff is 5 and 500 shells are divided to plot the radial distribution of average V_{ij}. Figure 15 shows the results for the high- and low-energy phases at $G_0 = 0.01$. It is clear that high-V_{ij} pairs more prefer to assemble within the nearest neighboring distance when the LLPT occurs.

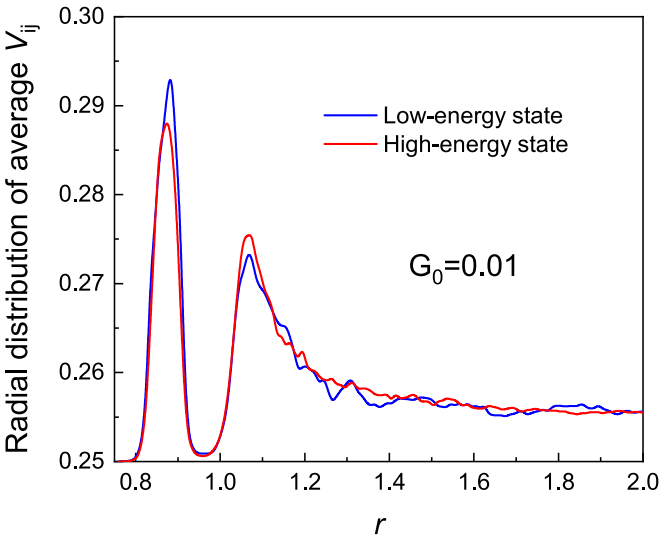

FIG. 15. Radial distribution of V_{ij} at $G_0 = 0.01$.

[1] C. Angell, J. Non-Cryst. Solids **131-133**, 13 (1991).
[2] C. Angell, Science **267**, 1924 (1995).
[3] P. G. Debenedetti and F. H. Stillinger, Nature (London) **410**, 259 (2001).
[4] H.-B. Yu, W.-H. Wang, and K. Samwer, Mater. Today **16**, 183 (2013).
[5] Q. L. Bi, Y. J. Lü, and W. H. Wang, Phys. Rev. Lett. **120**, 155501 (2018).
[6] L. Berthier and G. Biroli, Rev. Mod. Phys. **83**, 587 (2011).
[7] M. D. Ediger, Annu. Rev. Phys. Chem. **51**, 99 (2000).
[8] W. Kauzmann, Chem. Rev. **43**, 219 (1948).
[9] D. V. Matyushov and C. Angell, J. Chem. Phys. **123**, 034506 (2005).
[10] D. V. Matyushov and C. A. Angell, J. Chem. Phys. **126**, 094501 (2007).
[11] L. Xu, S. V. Buldyrev, N. Giovambattista, C. A. Angell, and H. E. Stanley, J. Chem. Phys. **130**, 054505 (2009).
[12] S. Sastry and C. Austen Angell, Nat. Mater. **2**, 739 (2003).
[13] J. C. Palmer, F. Martelli, Y. Liu, R. Car, A. Z. Panagiotopoulos, and P. G. Debenedetti, Nature (London) **510**, 385 (2014).
[14] L. Xu, P. Kumar, S. V. Buldyrev, S.-H. Chen, P. H. Poole, F. Sciortino, and H. E. Stanley, Proc. Natl. Acad. Sci. USA **102**, 16558 (2005).
[15] H. Tanaka, R. Kurita, and H. Mataki, Phys. Rev. Lett. **92**, 025701 (2004).
[16] R. Kurita and H. Tanaka, Science **306**, 845 (2004).
[17] Q. Cheng, Y. Sun, J. Orava, H. Bai, and W. Wang, Acta Mater. **230**, 117834 (2022).
[18] A. C. Barnes, L. B. Skinner, P. S. Salmon, A. Bytchkov, I. Pozdnyakova, T. O. Farmer, and H. E. Fischer, Phys. Rev. Lett. **103**, 225702 (2009).
[19] E. W. Fischer, Physica A **201**, 183 (1993).
[20] H. Tanaka, J. Chem. Phys. **111**, 3163 (1999).
[21] F. Turci, C. P. Royall, and T. Speck, Phys. Rev. X **7**, 031028 (2017).
[22] L. O. Hedges, R. L. Jack, J. P. Garrahan, and D. Chandler, Science **323**, 1309 (2009).
[23] G. Adam and J. H. Gibbs, J. Chem. Phys. **43**, 139 (1965).
[24] W. Kob and H. C. Andersen, Phys. Rev. E **51**, 4626 (1995).
[25] S. Nosé, J. Chem. Phys. **81**, 511 (1984).
[26] W. G. Hoover, Phys. Rev. A **31**, 1695 (1985).
[27] S. Plimpton, J. Comput. Phys. **117**, 1 (1995).
[28] L. Berthier, E. Flenner, C. J. Fullerton, C. Scalliet, and M. Singh, J. Stat. Mech. (2019) 064004.
[29] L.-H. Zhang and C.-H. Lam, Phys. Rev. B **95**, 184202 (2017).
[30] C.-S. Lee, M. Lulli, L.-H. Zhang, H.-Y. Deng, and C.-H. Lam, Phys. Rev. Lett. **125**, 265703 (2020).
[31] E. G. Teich, G. van Anders, and S. C. Glotzer, Soft Matter **17**, 600 (2021).
[32] S. A. Kube, S. Sohn, R. Ojeda-Mota, T. Evers, W. Polsky, N. Liu, K. Ryan, S. Rinehart, Y. Sun, and J. Schroers, Nat. Commun. **13**, 3708 (2022).
[33] Y. Cheng and E. Ma, Prog. Mater. Sci. **56**, 379 (2011).
[34] M. Hemmati, C. T. Moynihan, and C. A. Angell, J. Chem. Phys. **115**, 6663 (2001).
[35] S. Wei, F. Yang, J. Bednarcik, I. Kaban, O. Shuleshova, A. Meyer, and R. Busch, Nat. Commun. **4**, 2083 (2013).
[36] R. S. Singh, J. W. Biddle, P. G. Debenedetti, and M. A. Anisimov, J. Phys. Chem. C **144**, 144504 (2016).
[37] H. Tanaka, Phys. Rev. E **62**, 6968 (2000).
[38] C. U. Kim, B. Barstow, M. W. Tate, and S. M. Gruner, Proc. Natl. Acad. Sci. USA **106**, 4596 (2009).
[39] P. F. McMillan and M. C. Wilding, J. Non-Cryst. Solids **354**, 1015 (2008).
[40] M. Tanemura, T. Ogawa, and N. Ogita, J. Comput. Phys. **51**, 191 (1983).